

Transformation of magnetic data to the pole and vertical dip and a related apparent susceptibility transform: Exact and approximate approaches

Richard S. Smith¹, Eric A. Roots¹, and Rajesh Vavavur¹

ABSTRACT

The dipolar character of magnetic data means that there is a high and a low associated with each source. The relative positions and sizes of these highs and lows vary depending on the magnetic latitude or the inclination of the earth's magnetic field. One method for dealing with this complexity is to transform the data to what would be collected if the inclination were vertical (as at the magnetic pole), a process that is unstable at low magnetic latitudes. Unfortunately, remanent magnetization adversely impacts the success of this transformation. A second approach is to calculate the analytic-signal amplitude (ASA) of the data, which creates a single positive feature for each source or edge, with the shape being only weakly dependent on the inclination and the presence of remanent magnetization. The ASA anomalies can appear to be relatively broad,

so features sometimes merge together on map views of the ASA. A subsequent transformation of the ASA using an appropriate transforming tilt angle can generate a magnetic field of a body that is at the pole and has a vertical dip. The transformation is exact for contacts when calculated from the first-order ASA, but the sign of the transformed data can be incorrect depending on whether you are over one edge or the other edge of a discrete source body. Another approximate transformation of the zeroth-order ASA does not have this issue and gives good results on synthetic data provided that any noise is handled appropriately. The resulting maps outline the magnetic source bodies and have amplitudes proportional to an apparent magnetic susceptibility. On field data from Black Hill, South Australia, the approximate transformation generates an image that is simple to interpret and enhances some features less obvious on other enhancements of the data.

INTRODUCTION

Magnetic data are commonly used for interpreting the subsurface geology, with open-access digital textbooks devoting multiple chapters to this topic (Reeves, 2005; Isles and Rankin, 2013). One of the complexities of interpreting magnetic data is that the magnetic field is dipolar in nature, so every source body will have an anomaly with a positive part and a negative part; furthermore, the positions and relative sizes of these positive and negative parts vary depending on the inclination of the inducing earth's field (Reford, 1964; Reeves, 2005, pp. 8–11) and possible remanent magnetization. The inclination of the earth's field changes across the earth, depending on the magnetic latitude of the survey, so an experienced interpreter can get used to the positions and relative sizes in one part of the world but be less comfortable when looking at data collected in a part of the world with a different inclination.

One solution to this problem is to phase rotate the magnetic data to adjust the positions and relative sizes of the positive and negative parts to give the anomaly that would be measured at the pole. Baranov (1957) and Baranov and Naudy (1964) introduce a method to transform data in this way. However, the method can be unstable if the original data are collected close to the magnetic equator, so considerable effort has been expended on methods that stabilize this process (Silva, 1986; Arkani-Hamed, 1988; Hansen and Pawlowski, 1989; Mendonça and Silva, 1993; Keating and Zerbo, 1996; Lu, 1998; Li and Oldenburg, 2001; Lu et al., 2003; Arkani-Hamed, 2007; Guspi and Novara, 2009; Li et al., 2014). A further complication is that this reduction-to-the-pole (RTP) procedure assumes that all of the anomalies in the original data are associated with fields oriented in the direction of the inducing field. If there are any anomalies with strong remanent magnetization, such that the total magnetization is not in the assumed direction, then the amount

Manuscript received by the Editor 18 November 2020; revised manuscript received 7 October 2021; published ahead of production 4 December 2021; published online 24 January 2022.

¹Laurentian University, Harquail School of Earth Sciences, Sudbury, Ontario P3E 2C6, Canada. E-mail: rsmith@laurentian.ca (corresponding author); eroots@laurentian.ca; rvavavur@laurentian.ca.

© 2022 Society of Exploration Geophysicists. All rights reserved.

of phase rotation will be incorrect and the transformed anomaly will not look like an anomaly at the pole (Li et al., 2021). This can be a greater problem close to the magnetic equator, as the earth's field strength is weaker, so the induced field will be weaker, and a relatively small remanent magnetization will be able to rotate the total magnetization a greater angle from the assumed direction. If the RTP process is successful, a compact body will generally have a symmetric positive anomaly over the body and a small negative around the outside of the body. This gives an anomaly that can be easier to interpret as it is positive over the body. However, this is only the case when the edge of the body has a vertical dip. If the edge of the body dips, then the positions and the relative sizes of the positive and negative peaks can change.

A second solution is to calculate the first-order analytic-signal amplitude (ASA_1) of the magnetic data (Nabighian, 1972) given by

$$ASA_1 = \sqrt{\left(\frac{\partial H}{\partial x}\right)^2 + \left(\frac{\partial H}{\partial z}\right)^2}, \quad (1)$$

where H is the magnetic field and the two squared terms are the horizontal (x) derivative and the vertical (z) derivative of the magnetic field, respectively. The quantity ASA_1 is independent of the dip and magnetic latitude for 2D structures (Nabighian, 1972) and weakly dependent on the magnetic inclination and dip for 3D structures (Roest et al., 1992; Rajagopalan, 2003). MacLeod et al. (1993) show that the shape of the first-order ASA (ASA_1) was largely independent of any remanent magnetization. For this reason, ASA_1 is commonly used to transform data close to the pole or to transform data that display strong remanent magnetization into a form that can be used for interpretation.

A weakness with imaging and interpreting ASA_1 is that this quantity is the root mean square (rms) of the vertical and horizontal derivatives. These derivatives are large over lateral changes in magnetization such as edges and will be small over constantly magnetized parts of a body. Hence, over the center of a uniformly magnetized body, ASA_1 is small, whereas over the edges, ASA_1 is large. Hence, this quantity is good for identifying edges, but not the bodies or the susceptibilities in between the edges. One solution to this is to use a zeroth-order ASA (ASA_0), which is the rms of the total field and its Hilbert transform in the horizontal direction:

$$ASA_0 = \sqrt{H^2 + \bar{H}_x^2}, \quad (2)$$

where the horizontal bar denotes the Hilbert transform of H and the subscript tells us that the transform is in the x -direction. The quantity ASA_0 has a value proportional to the susceptibility over the top of the bodies and can be used for interpreting susceptibility and possibly lithology. However, ASA_0 decreases slowly away from the edges of bodies, so the anomalies are very broad and the precise location of the edges is difficult to interpret.

A third alternative is to use the first- or second-order local wavenumbers (Thurston and Smith, 1997; Smith et al., 1998), but like ASA_1 , these also highlight edges and the local wavenumbers are only dependent on the depth and structural index of the source, so any susceptibility information is lost.

In this contribution, we propose a new alternative transformation that can give a field that is independent of the magnetic inclination,

dip, and the direction of any remanent magnetization, and can be used to estimate the magnetic susceptibility.

THEORY

For a magnetic field $H(x, z)$, the first-order analytic signal is defined as (Nabighian, 1972)

$$A_1 = \frac{\partial H}{\partial x} + i\left(-\frac{\partial H}{\partial z}\right), \quad (3)$$

which is a complex quantity, where the real part is the horizontal (x) derivative of the magnetic field and the imaginary part is the negative of the vertical (z) derivative. Nabighian (1972) shows that these two parts are a Hilbert transform pair for the case of a 2D dipping contact. It is sometimes convenient to represent this complex number by its amplitude, called the first-order ASA and defined in equation 1, and the first-order tilt angle, denoted as T_1 , where

$$T_1 = \tan^{-1}\left(\frac{\partial H}{\partial z} / \frac{\partial H}{\partial x}\right). \quad (4)$$

The graphical relationship between the real and imaginary parts of the analytic signal and the first-order tilt T_1 is shown in Figure 1a.

Note that the tilt angle T_1 is the same as the quantity used by others, called the potential-field tilt by Miller and Singh (1994) and the local phase by Thurston and Smith (1997). For the case of the dipping contact, the first-order tilt T_1 is given by (Cooper, 2016, his equation 5)

$$T_1 = \tan^{-1}\left(\frac{\Delta x \cos \beta - \Delta z \sin \beta}{\Delta z \cos \beta + \Delta x \sin \beta}\right), \quad (5)$$

where $\beta = 2I - d - \pi/2$, I is the inclination of the earth's field, d is the dip of the contact, and Δx and Δz are the distances from the measurement point to the top of the body in the x - and z -directions, respectively. If the location is at the pole, then the inclination I is 90° ($\pi/2$ radians), and if the dip d is also 90° , then $\beta = 0$ and Salem et al. (2007) obtain the simple expression:

$$T_1 = \tan^{-1}\left(\frac{\Delta x}{\Delta z}\right). \quad (6)$$

This expression is important, not for estimating the location of the contact when $\Delta x = 0$, or the depth Δz , but, as we will show, for using the first-order tilt T_1 to reconstruct the magnetic field or its derivative when $\beta = 0$.

Cooper (2016, his equation 22) extends the concept of a tilt calculated from the components of the complex analytic signal, as outlined previously, to the equivalents calculated from an ASA. He defines the tilt of the N th-order ASA for a 2D body by the following expression:

$$T_{ASA_N} = \tan^{-1}\left(\frac{\partial ASA_N}{\partial z} / \frac{\partial ASA_N}{\partial x}\right). \quad (7)$$

The graphical relationship between the two spatial derivatives of the N th-order ASA and the N th-order ASA tilt T_{ASA_N} is shown

in Figure 1b. The triangles are drawn to be different sizes in Figure 1 to make clear that these two tilt angles are not always the same. Furthermore, in his appendix, Cooper (2016) shows that this expression becomes

$$T_{ASA_N} = \tan^{-1} \left(\frac{\Delta z}{\Delta x} \right), \quad (8)$$

for the cases of a contact ($N = 1$) and a dike ($N = 2$). In fact, this expression is also true for $N = 3$, the case of a horizontal cylinder (MacLeod et al., 1993).

One of the advantages of the ASAs and the associated tilts is that Cooper (2019) shows that the vertical derivative of the magnetic field $\partial H(x, y)/\partial z$ can be obtained from the first-order ASA₁ and the first-order tilt angle T_1 :

$$\frac{\partial H}{\partial z} = ASA_1 \sin(T_1), \quad (9)$$

except that for maps rather than profiles, the first-order tilt T_1 is given by the expression

$$T_1 = \tan^{-1} \left(\frac{\partial H/\partial z}{\sqrt{(\partial H/\partial x)^2 + (\partial H/\partial y)^2}} \right). \quad (10)$$

The definition of T_1 in equation 10 is very similar to the definition of the profile case in equation 4, except that the derivative in the x -direction in equation 4 has been replaced by the rms of the derivatives in the x - and y -directions, respectively.

Similarly, Cooper (2019) shows that the magnetic field on a grid $H(x, y)$, where x and y are the eastings and northings, can be obtained from the amplitude of the zeroth-order ASA₀ and the zeroth-order tilt angle T_0 , namely,

$$H = ASA_0 \sin(T_0), \quad (11)$$

where on a grid equation 2 becomes

$$ASA_0 = \sqrt{H^2 + \bar{H}_x^2 + \bar{H}_y^2}, \quad (12)$$

and the zero-order tilt T_0 is now

$$T_0 = \tan^{-1} \left(\frac{H}{\sqrt{\bar{H}_x^2 + \bar{H}_y^2}} \right), \quad (13)$$

where the bar and subscripts in \bar{H}_x and \bar{H}_y denote the Hilbert transforms of $H(x, y)$ in the two horizontal directions, x and y , respectively.

Hence, knowing the relevant ASA and tilt, Cooper (2019) shows that it is possible to reconstruct the total field or its vertical derivative at the location they were measured.

In this paper, we seek to reconstruct the vertical derivative and total field, not as they were actually measured but as if they were measured at the pole and when the dips are vertical ($\beta = 0$). This should give fields that are not phase rotated by a nonvertical inclination of the earth's field or by any remanent magnetization that has a component perpendicular to the earth's magnetic field.

When reconstructing the vertical derivative for $\beta = 0$ using equation 9, the first-order tilt T_1 would be given in equation 6, but this tilt, $T_1^{\beta=0}$, is not measured. However, the argument of the \tan^{-1} function in equation 6 is the inverse of the argument in the same function given in equation 8, which is the ASA tilt, T_{ASA_N} , and this quantity can be calculated from a measured field using equation 7. Taking the tangent of both sides of equation 6 and 8, for the case when $\beta = 0$, we obtain the expression

$$\tan T_{ASA_N} = \frac{1}{\tan(T_1^{\beta=0})} = \cot(T_1^{\beta=0}). \quad (14)$$

However, using the well-known trigonometric cofunction reflection identity $\cot \theta = \tan(\frac{\pi}{2} - \theta)$, we obtain

$$\tan T_{ASA_N} = \tan\left(\frac{\pi}{2} - T_1^{\beta=0}\right), \quad (15)$$

and then taking the inverse tangent of both sides obtains

$$T_1^{\beta=0} = \frac{\pi}{2} - T_{ASA_N}. \quad (16)$$

Equation 16 is used to calculate the desired quantity, the first-order tilt $T_1^{\beta=0}$, for the specific case of a field at the pole with vertical dip ($\beta = 0$ case). The quantity T_{ASA_N} on the right side is calculated from the known ASA using equation 7. In this paper, we use ASA₁ because this quantity will contain less high-frequency noise than the higher-order analytic signals. This subtraction of the ASA tilt angle T_{ASA_N} from $\pi/2$ is here called a *phase reflection*. We can calculate the vertical derivative of the field of a body at the pole that has vertical dips ($\beta = 0$) using a modified form of equation 9:

$$\frac{\partial H}{\partial z} = ASA_1 \sin(T_1^{\beta=0}). \quad (17)$$

As the total magnetization is rotated to vertical, remanent magnetization will not adversely impact the phases on the final image. The vertical derivative can then be vertically integrated in the Fourier domain to give the magnetic field at the pole with vertical dips.

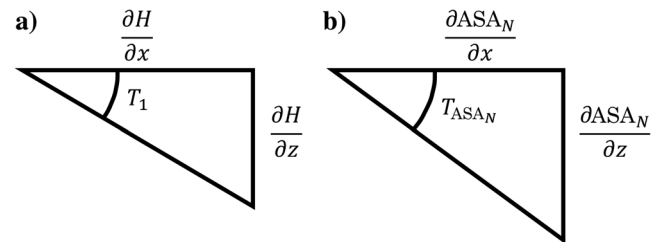


Figure 1. (a) The relation between the first-order tilt T_1 and the two components of the complex analytic signal, $\partial H/\partial x$ and $\partial H/\partial z$. (b) The relation between the ASA tilt T_{ASA_N} and the two spatial derivatives of the N th-order ASA, $\partial ASA_N/\partial x$ and $\partial ASA_N/\partial z$, which are discussed in the text.

SYNTHETIC PROFILE EXAMPLES

Transformation to the vertical derivative at the pole with vertical dip

The first example considered is the case of a contact model, for which the preceding theory has been derived. The derivative of the magnetic field of a contact is calculated using the semi-infinite block model of Nabighian (1972). Figure 2a shows the vertical derivative (dotted-dashed blue line), horizontal derivative (dotted orange line), and first-order ASA (dashed green line) for the case when the magnetic field is 55,000 nT and is vertical (at the pole). Figure 2b shows the first-order tilt (dotted-dashed blue line), and the tilt for the case of vertical dip, $T_1^{\beta=0}$, is shown with the dotted orange line. In this example, we chose a magnetic inclination of 90° so the reader could verify that these two tilts are very similar for negative distances but differ by 2π for positive distances. However, trigonometric functions are the same for arguments that differ by $n2\pi$ (where $n = 0, \pm 1, \pm 2, \dots$), so these tilts are essentially the same after the sines of the tilts are taken in equation 17. In fact, the vertical derivative calculated using $T_1^{\beta=0}$ in equation 17 is plotted with the solid red line in Figure 2a. This red line is identical to the actual vertical derivative, so it obscures the dotted-dashed blue line. This diagram illustrates that the preceding theory applies for the simple case of a contact model.

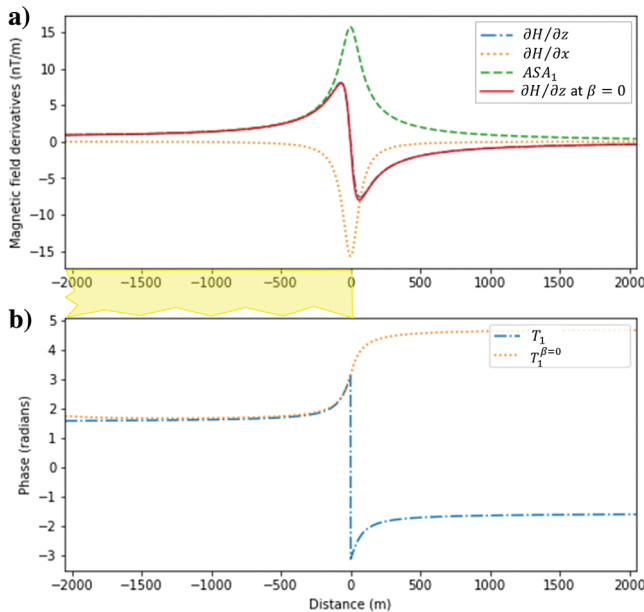


Figure 2. (a) The vertical derivative ($\partial H/\partial z$) and horizontal derivative ($\partial H/\partial x$), and first-order ASA (ASA_1) for a 2D vertical contact at the origin and comprising susceptible material (0.01 SI) extending infinitely to the left and to depth, denoted by the yellow transparent body below the horizontal axis. The sensor height is 70 m above the top of the body. The earth's magnetic field intensity is 55,000 nT and the inclination is 90° . The orientation of this and subsequent profiles is north-south. (b) The first-order tilt (T_1 , calculated from equation 4) and the first-order tilt for the case when $\beta = 0$, denoted $T_1^{\beta=0}$, calculated from equation 16. Substituting $T_1^{\beta=0}$ into equation 17, we obtained the vertical derivative transformed to the pole and vertical dip shown in (a) with the solid red line and labeled " $\partial H/\partial z$ at $\beta = 0$."

However, most magnetic anomalies are not associated with bodies that are semi-infinite. Many anomalies considered by geophysicists are finite in extent and thus better represented by a body with two edges. The second example is the case of a block model constructed by subtracting a semi-infinite sheet with an edge at +500 m from one with an edge at -500 m. Figure 3a shows these fields for the case when the inducing field is vertical with a strength of 55,000 nT. The vertical derivative is shown with the dotted-dashed blue line, the horizontal derivative is the orange dotted line, and ASA_1 is calculated as the rms of these two derivatives and is shown with the dashed green line. Note that the ASA_1 anomaly is broader than the positive vertical derivative anomaly. The first-order tilt T_1 is shown in Figure 3b as a dotted-dashed blue line, whereas the tilt of the first-order ASA, T_{ASA_1} after reflection is shown with the dotted orange line as $T_1^{\beta=0}$. When the latter tilt is used in equation 17 to transform the ASA_1 to the vertical derivative for the case $\beta = 0$, we get the red line in Figure 3a. We might expect that this will be similar to the original vertical derivative because our initial model satisfied the $\beta = 0$ condition. They are very similar for positive x , but they are the negative of each other for negative x .

We conclude that the method is able to detect the edges of the contact, but it is unable to distinguish between the left and right edges. This is because, for one edge, the right side has a positive susceptibility contrast with the background, and for the other edge

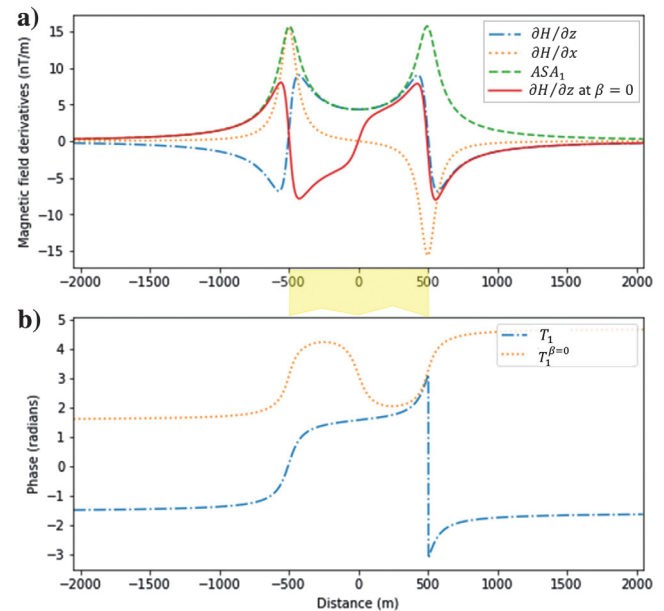


Figure 3. (a) The vertical derivative ($\partial H/\partial z$) and horizontal derivative ($\partial H/\partial x$), and first-order ASA (ASA_1) for a body extending to infinite depth, but with two edges, one at -500 m and a second at +500 m, denoted by the yellow transparent body below the horizontal axis. The sensor height is 70 m above the top of the body. The earth's magnetic field intensity is 55,000 nT and the inclination is 90° . The orientation of the profile is north-south. (b) The first-order tilt (T_1 , calculated from equation 4) and the first-order tilt for the case when $\beta = 0$, denoted $T_1^{\beta=0}$, calculated from equation 16. Substituting $T_1^{\beta=0}$ into equation 17, we obtained the vertical derivative transformed to the pole and vertical dip shown in (a) with the solid red line and labeled " $\partial H/\partial z$ at $\beta = 0$." For a body with two edges, the solid red and dotted-dashed blue lines in (a) do not agree on the left side.

the right side has a negative susceptibility contrast. This sign information is retained when calculating the vertical and horizontal derivatives over either edge, but it cancels out and is lost taking the ratio of the two derivatives when calculating the phase (equation 4) and is also lost from the ASA (equation 1) when the two derivatives are squared. Hence, the tilts and ASAs and the subsequent formulas they are substituted into do not contain the information as to whether it is an edge with a positive or negative susceptibility contrast. However, it is possible to use other means to identify the left and right edges of a body. We estimated the center x_c of the ASA_1 anomaly using the formula

$$x_c = \frac{\int ASA_1 x dx}{\int ASA_1 dx}, \quad (18)$$

where the limits of the integral are the left and right ends of the profile. If we multiply $T_1^{\beta=0}$ by negative unity for $x < x_c$ and positive unity for $x > x_c$, we get the result in Figure 4, which is closer to the desired result, having the correct sign over both edges. However, there is a cusp in the transformed vertical derivative (red curve) close to the center of the anomaly. This is halfway between the two edges, which is the point closest to both edges, where any interference effects between these two edges will be greatest.

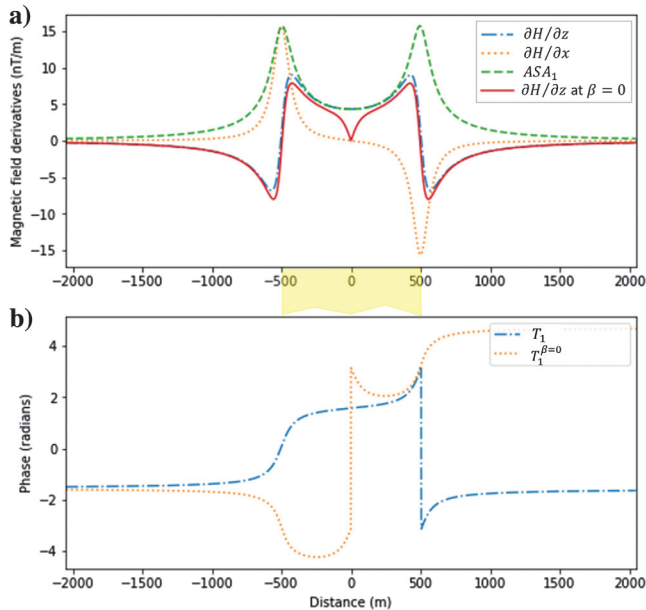


Figure 4. (a) The vertical derivative ($\partial H/\partial z$) and horizontal derivative ($\partial H/\partial x$), and first-order ASA (ASA_1) for a body extending to infinite depth, but with two edges, one at -500 m and a second at $+500$ m, denoted by the yellow transparent body below the horizontal axis. The sensor height is 70 m above the top of the body. The earth's magnetic field intensity is $55,000$ nT and the inclination is 90° . The orientation of the profile is north-south. (b) The first-order tilt (T_1 , calculated from equation 4) and the first-order tilt for the case when $\beta = 0$, denoted $T_1^{\beta=0}$, calculated from equation 16 but negated to the left of the center of the anomaly. Substituting this $T_1^{\beta=0}$ into equation 17, we obtained the vertical derivative transformed to the pole and vertical dip shown in (a) with the solid red line and labeled " $\partial H/\partial z$ at $\beta = 0$."

As this anomaly is symmetric, it is easy to identify the center of the anomaly, so we can null or remove values impacted by interference within 150 m of the center of the anomaly (or the middle 30% of the body) and then replace them with nearby values.

This has been done in Figure 5 and the transformed vertical derivative (red line) is as we expect, looking very similar to the vertical derivative for the $\beta = 0$ case of Figure 3. However, in Figure 5, the vertical and horizontal derivatives are quite different. This is because we changed the inclination of the earth's field to 22.5° , so $\beta \neq 0$. This was done to demonstrate that the transformed field is independent of the value of β for the initial data. The manual editing we did around the center of the anomaly means that the result has a flat zone and is therefore slightly approximate for a body with two edges. Gentle filtering could remove this flat feature.

The necessity to change the sign for portions of the data and to null values and replace them with interpolated values makes transformation of the data to the vertical derivative for the case $\beta = 0$ somewhat problematic. We spent some time experimenting with other means to solve this problem, including using different ways of calculating the tilt, but none of them solved the problem.

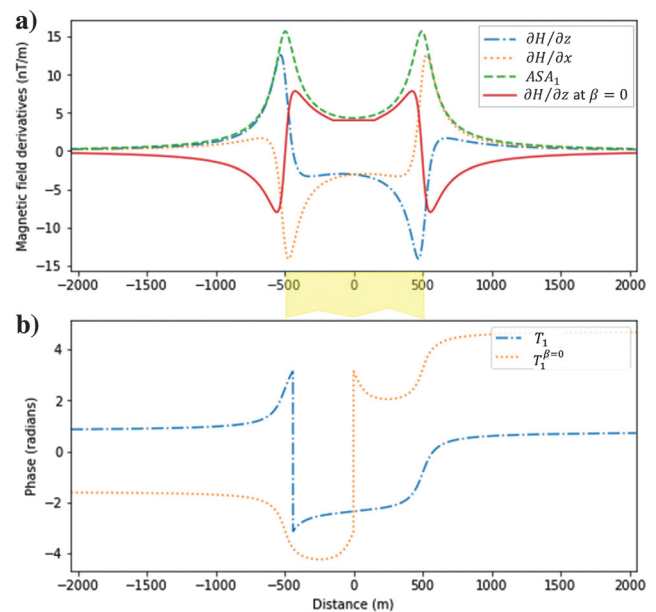


Figure 5. (a) The vertical derivative ($\partial H/\partial z$) and horizontal derivative ($\partial H/\partial x$), and first-order ASA (ASA_1) for a body extending to infinite depth, but with two edges, one at -500 m and a second at $+500$ m, denoted by the yellow transparent body below the horizontal axis. The sensor height is 70 m above the top of the body. The earth's magnetic field intensity is $55,000$ nT and the inclination is changed to 22.5° . The orientation of the profile is north-south. (b) The first-order tilt (T_1 , calculated from equation 4) and the first-order tilt for the case when $\beta = 0$, denoted $T_1^{\beta=0}$, calculated from equation 16 but negated to the left of the center of the anomaly. Substituting this $T_1^{\beta=0}$ into equation 17, we obtained the vertical derivative transformed to the pole and vertical dip shown in (a) with the solid red line and labeled " $\partial H/\partial z$ at $\beta = 0$ "; however, the cusp at the center of Figure 4a has been removed by editing the data. Also, note that the change in inclination changes the vertical and horizontal derivatives, but the ASA and the basic shape of the transformed field (red) have not changed.

Transformation to the total field at the pole with vertical dip

The total field can be reconstructed using equation 11, but there is no expression for the tilt T_0 analogous to equation 8 when $\beta = 0$. By analogy with the equality of different-order tilts $T_{ASA_3} = T_{ASA_2} = T_{ASA_1}$, for the cases of the horizontal cylinder, thin dike, and contact (MacLeod et al., 1993; Cooper, 2016), we can assume that T_{ASA_0} could yield a comparable value, so we calculate T_{ASA_0} from the expression

$$T_{ASA_0} = \tan^{-1} \left(\frac{\partial ASA_0}{\partial z} / \sqrt{(\partial ASA_0 / \partial x)^2 + (\partial ASA_0 / \partial y)^2} \right). \quad (19)$$

Calculating the vertical derivative of ASA_0 requires an upward continuation of the field a small distance (e.g., 10 m) to calculate ASA_0 at two heights; the horizontal derivative can be calculated by a finite difference. To recover a quantity similar to the total field, we found that a phase reflection of $(\pi/2) - T_{ASA_0}$ was not required, but that a reversal in sign was necessary, so that the tilt used in equation 11 becomes

$$T_0^{\beta=0} = -T_{ASA_0}. \quad (20)$$

As an example, we take the same model as Figure 3 and calculate the fields and transformed fields. Figure 6 shows the original total

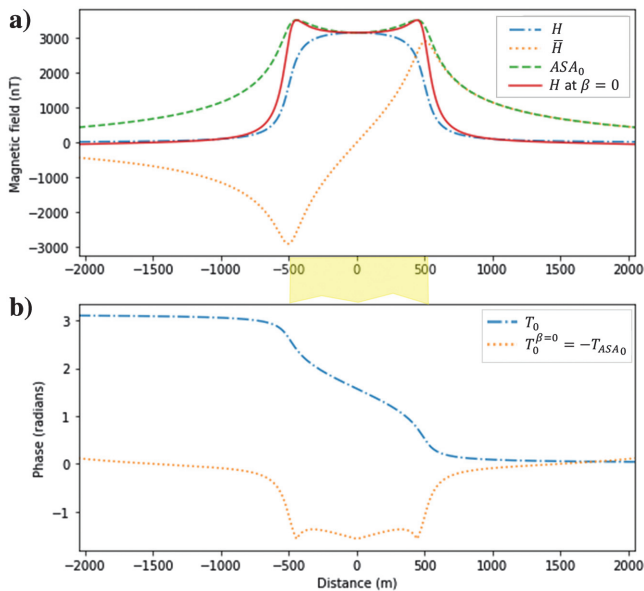


Figure 6. (a) The total field (H), Hilbert transform of the total field (\hat{H}), and the zeroth-order ASA (ASA_0) for a thick magnetic body extending to infinite depth with edges at ± 500 m (yellow transparent block), a susceptibility of 0.01 SI, and a sensor height 70 m above the top of the body. The earth's magnetic field intensity is 55,000 nT and the inclination is 90° . The profile is north-south. The zeroth-order tilt T_0 and zeroth-order ASA tilt after negation so as to give $T_0^{\beta=0}$ are shown in (b). The magnetic field transformed to the pole and vertical dip (H at $\beta = 0$) shown in (a) is calculated using equation 11, which requires as input ASA_0 and $T_0^{\beta=0}$, defined in equation 20.

field (dotted-dashed blue line) in Figure 6a and its Hilbert transform (dotted orange line) and the ASA_0 , which is the rms of these two quantities (dashed green line). The zeroth-order tilt T_0 is shown as a dotted-dashed blue line in Figure 6b and the tilt of the ASA, T_{ASA_0} , after negation for the $\beta = 0$ case is shown as the orange line. When this latter tilt is used in equation 11, we get the red line in Figure 6a. Note that this is similar in magnitude but is less rounded than the original total magnetic field (dotted-dashed blue line) with two small peaks near the edge. Hence, this transform is not exact and also is approximate.

To demonstrate that this transformation is independent of β (dip or magnetic inclination), we have recalculated these quantities for the case when the magnetic inclination is 22.5° , and we get the curves in Figure 7. The magnetic field (and its Hilbert transform) is asymmetric and predominantly negative, but ASA_0 (dashed green line) and the transformed field (solid red line) are largely symmetric and positive. The transformed magnetic field anomaly is sharper and narrower than the ASA_0 .

The tilts show a slight distortion of the results at large offsets on the extreme left and right of the plot. This is due to the fact that the fast Fourier transform (FFT) is used to calculate the Hilbert transform and the FFT assumes that the profile repeats periodically. This periodic repetition results in discontinuities in the fields at the edges of the profile and these can propagate away from the edges when a wide operator (such as a Hilbert transform) is applied to the data. These distortions have been minimized by applying a Tukey window, with 50% of the data being unaffected and 50% having a cosine taper applied to ensure there is no discontinuity at the edges. The actual series

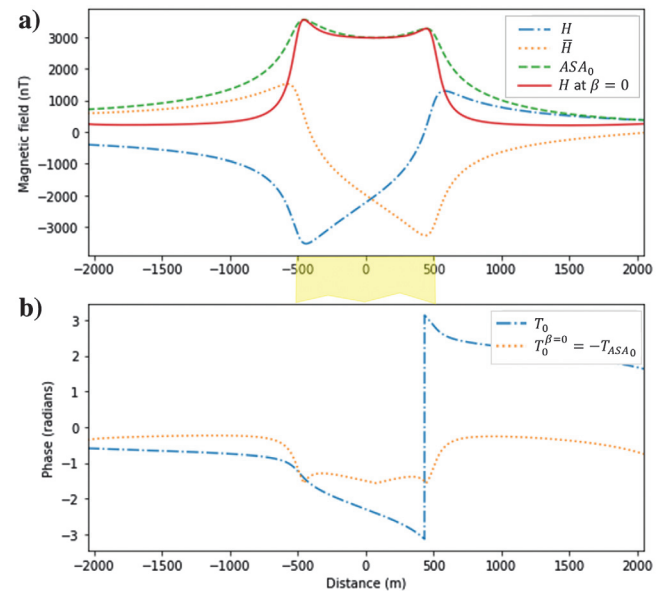


Figure 7. (a) The total field (H), Hilbert transform of the total field (\hat{H}), and the zeroth-order ASA (ASA_0) for a thick magnetic body extending to infinite depth with edges at ± 500 m (yellow transparent block), a susceptibility of 0.01 SI, and a sensor height 70 m above the top of the body. The earth's magnetic field intensity is 55,000 nT and the inclination has been changed to 22.5° . The profile is north-south. The zeroth-order tilt T_0 and zeroth-order ASA tilt after negation so as to give $T_0^{\beta=0}$ are shown in (b). The magnetic field transformed to the pole and vertical dip (H at $\beta = 0$) shown in (a) is calculated using equation 11, which requires as input ASA_0 and $T_0^{\beta=0}$, defined in equation 20.

used went from -4096 to $+4096$, but the data between ± 2048 are unaffected by the cosine taper.

APPARENT SUSCEPTIBILITY ESTIMATION

As the magnetic data have been reduced to the pole and vertical dip, it is possible to convert the data to a susceptibility assuming a model with two contact-like edges by dividing by $2\pi Fc$ (Nabighian, 1972), where F is the magnetic field intensity, c is the coupling factor given by $c = 1 - \cos^2 I \sin^2 A$, I is the inclination, and A is the angle between the direction perpendicular to strike and magnetic north. The 2π factor is a consequence of the fact that a magnetic contact with one edge has an anomaly that goes from a minimum of $-\pi kFc$ to a maximum of $+\pi kFc$ so a body with two edges will go from zero to $2\pi kFc$. Because the transformed data have $\beta = 0$, the transform rotates any magnetization to vertical. Hence, this susceptibility is an apparent susceptibility that would explain the total magnetization in the case when remanent magnetization is present. The $2\pi Fc$ normalization factor does not take into account the distance between the source and sensor, so the apparent susceptibility value is the susceptibility of a two-edged block with infinite depth extent and its top at the height of the sensor. This will be an underestimate of the susceptibility unless the data have been downward continued to the height of the source.

The magnetic field can be derived from equation 11, but it can also be derived from the vertical derivative by undertaking a vertical integration in the Fourier domain, where the operator for the integral is the inverse of the absolute value of the wavenumber (in radians), which is the inverse of the derivative operator. Figure 8 shows the apparent susceptibility derived from the magnetic field data

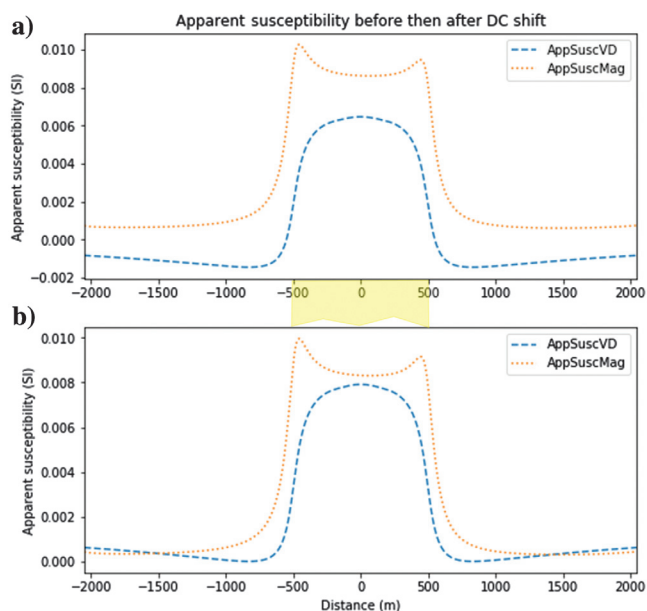


Figure 8. Apparent susceptibility calculated by two methods. The dotted orange line is from the transformed magnetic field (AppSuscMag) using equation 11, with the tilt defined in equation 20 and the dashed blue line is the magnetic field vertically integrated from the transformed vertical derivative (AppSuscVD). The constant of integration is unknown, being set to zero in (a) and set to a value to ensure no negative magnetic susceptibilities in (b). The location of the body is marked by the yellow transparent block on (a) only.

estimated using both these methods. The vertical integration has an unknown constant of integration, which is typically set to zero (Figure 8a). This results in a large number of strongly negative susceptibilities, which is not possible, so adding a constant to ensure no negative susceptibilities gives the results in Figure 8b. The susceptibility is within 20% of the model value (0.01 SI). Downward continuing the data or, equivalently, recalculating the model with a lower sensor height (1 m) returns values much closer to the model value (Figure 9).

SYNTHETIC EXAMPLES WITH NOISE APPLIED

To show the impact of noise, we have transformed ASA_0 to a total field and then calculated the apparent susceptibility when several different noise levels have been applied to the data. Figure 10a shows the magnetic-field response for the same model that we have used above at five different magnetic inclinations: 90° , 67.5° , 45° , 22.5° , and 0° . Each subsequent plot has the baseline offset by 1000 nT so that the different profiles are easier to recognize. The profiles clearly have different shapes and symmetries at different inclinations. Random noise was generated using the Python random noise generator, but this noise is white, with high-frequency content, so it was then filtered with a triangular filter to give wavelengths of approximately 40 m, which is comparable to the wavelengths that might be observed in aeromagnetic data. The 90° case is not corrupted with noise, but the subsequent curves are corrupted with increasing noise levels, corresponding to noise values between ± 2 , ± 4 , ± 8 , and ± 16 nT. These noise levels are larger than typical noise levels in compensated aeromagnetic data, which are generally of the order of 1 nT. The noise clearly impacts the apparent susceptibility curves in Figure 10b, with the results being more erratic in areas where the signal strength is weaker. The impact of the noise can be reduced by applying soft thresholding (Donoho, 1995) to the vertical and horizontal derivatives prior to calculating the inverse tangent. The soft thresholding replaces a value a with a compressed value \tilde{a} :

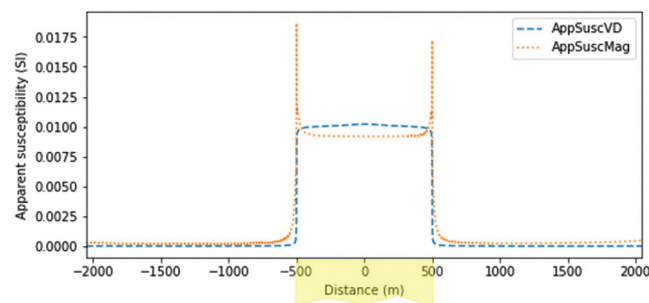


Figure 9. Apparent susceptibilities calculated in the case when the sensor height is 1 m above the ground and the constant of integration is set to an appropriate value for the susceptibility derived from the vertical derivative. The location of the body is marked by the yellow transparent block. Here, AppSuscVD is the apparent susceptibility from the vertical derivative transformed to the pole and vertical dip and then vertically integrated, and AppSuscMag is the apparent susceptibility derived from the magnetic field transformed to the pole and vertical dip (using equation 11, with the tilt defined in equation 20). The value over the body is very close to the true value of 0.01 SI.

$$\tilde{a} = \begin{cases} \text{sign}(a)(|a| - \text{thr}), & |a| > \text{thr} \\ 0, & |a| \leq \text{thr} \end{cases}, \quad (21)$$

where thr is the threshold value. Using a threshold value of 1.0 removes most of the erratic results (Figure 11), but all of the erratic values can be removed with thr = 2.0. Making thr too large can result in the profile being suppressed to zero in areas where the derivatives are small, but there is otherwise strong signal, such as in the center of the anomaly.

From these noise studies, we conclude that the methodology is impacted by noise, but it is possible to reduce the impact of noise typically encountered in magnetic surveys using soft thresholding. Figure 10b also demonstrated that transforming from the zeroth-order analytic signal effectively gives the same RTP and vertical-dip field when transformed from multiple different magnetic inclinations.

SYNTHETIC EXAMPLES ON 2D GRIDDED DATA

Due to the difficulties with identifying the appropriate sign on different edges when using the first-order analytic-signal method, we have elected to implement the zeroth-order analytic-signal method on gridded data. The two peaks near the edges of the transformed total field anomaly will mean that the transform is only approximately similar to the magnetic field; however, the characteristics of the resulting image mean that the image is well suited for

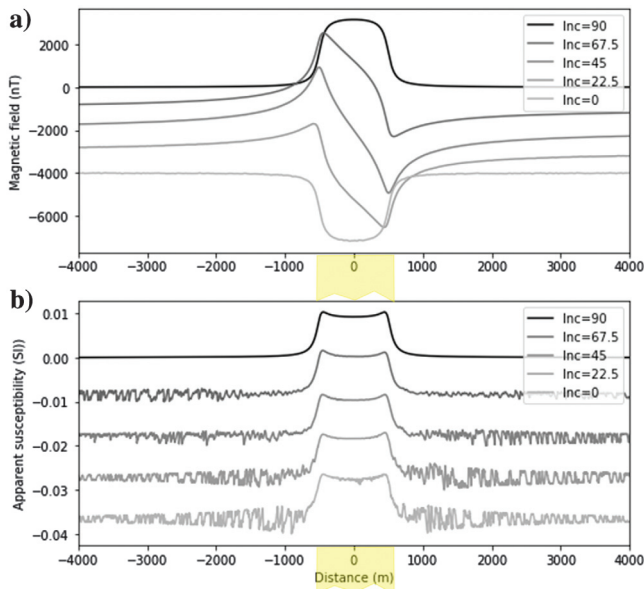


Figure 10. (a) Magnetic profiles at five inclinations, with baselines offset by 1000 nT to allow each profile to be viewed separately. The profiles from top to bottom are at inclinations of 90°, 67.5°, 45°, 22.5°, and 0° and are corrupted by noise with peak amplitudes of 0, ±2, ±4, ±8, and ±16 nT, respectively. (b) The apparent susceptibility derived from the five profiles by transforming the ASA₀ (using equation 11, with the tilt defined in equation 20), which in each case has similar symmetric shapes. The impact of increasing noise is evident in areas where the anomalies are weaker. The location of the body is marked by the yellow transparent block below the horizontal axes.

qualitative interpretation: specifically, interpreting edges, identifying anomalous bodies, and estimating apparent susceptibilities.

The procedure for calculating the field for the $\beta = 0$ case from map data and the associated apparent susceptibility map is as follows:

- 1) Calculate the Hilbert transforms in the x - and y -directions from the total field using the appropriate wavenumber-domain filters given in Nabighian (1984).
- 2) In the space domain, combine these with the total field to give ASA₀ (using equation 12).
- 3) Upward continue the total field using the upward continuation operator in the wavenumber domain (Dean, 1958).
- 4) Calculate the Hilbert transforms of the upward continued field as in step 1.
- 5) In the space domain, combine the upward continued total field and its Hilbert transforms to give the zeroth-order ASA at the upper height as in step 2.
- 6) In the space domain, subtract the zeroth-order ASA at the upper height from that at the lower height and divide by the height difference to give the vertical derivative of ASA₀ using a forward-difference approximation (Abramowitz and Stegun, 1972, their equation 25.1.1).
- 7) Estimate the x - and y -directed horizontal derivatives of ASA₀ in the space domain using finite differences (Abramowitz and Stegun, 1972). The height of the ASA₀ for which horizontal derivatives are taken could be the lower height or the midpoint between the two heights, depending on whether the vertical derivative is considered to be a forward difference or a central difference; however, we expect that the two results should be fairly similar. Finally, calculate the rms of these two horizontal derivatives to give the absolute value of the total horizontal derivative:

$$\frac{\partial \text{ASA}_0}{\partial h} = \sqrt{\left(\frac{\partial \text{ASA}_0}{\partial x}\right)^2 + \left(\frac{\partial \text{ASA}_0}{\partial y}\right)^2}. \quad (22)$$

- 8) Multiply the zeroth-order ASA by the sine of the appropriate transforming zeroth-order tilt (using equation 11): in this case, the appropriate tilt angle is $T_0^{\beta=0} = -T_{\text{ASA}_0}$, with T_{ASA_0} being derived from the ratio of the vertical to total horizontal derivatives of ASA₀ (steps 6 and 7, respectively)

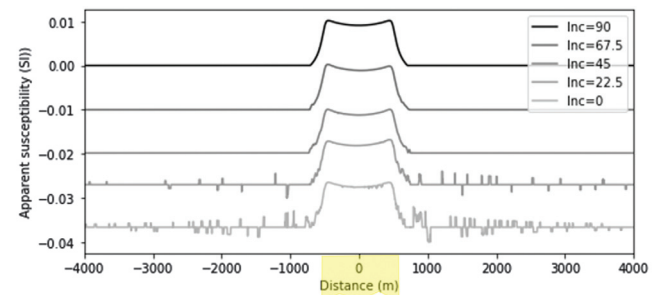


Figure 11. The apparent susceptibility derived from the five profiles in Figure 10a by transforming the ASA₀, except the soft threshold (equation 21) has been set to 1.0. Using a soft threshold value of 2.0 essentially removes all the noise from all curves. The location of the body is marked by the yellow transparent block.

and calculated using equation 19. If necessary, apply soft thresholding to the vertical and horizontal derivatives of ASA_0 to reduce any noise. Some experimentation might be required to select the right threshold value. The final result is the reduced-to-pole and vertical dip image, which can then be scaled or normalized by $2\pi Fc$ to also give the apparent susceptibility image, the two required maps.

These are all straightforward processes for manipulating magnetic data. The only potential pitfall is ensuring that the grid is extended and tapered to zero on the edges so that large anomalies from one side of the grid do not wrap around and extend into the other side of the grid due to the periodic assumption that is made when using the discrete Fourier transform to the wavenumber domain. This is particularly important, because the Hilbert transform filter is very broad. In the synthetic example discussed next, the grid is extended on all sides to 22 km away from the center of the grid, where the synthetic anomalies were effectively zero. In the field example, the grid size was doubled and the data were mirror imaged horizontally and vertically about the points on the extreme edges of the original grid and then tapered to zero with a cosine taper.

Synthetic data to test the preceding procedure have been generated using the Python geoscience modeling and interpretation package called PyGMI written by Patrick Cole (Cole, 2021). The magnetic field in the area was selected to be typical of that in South Australia, with a field strength of 50,000 nT, an inclination of -60° (Southern Hemisphere), and a declination of 5° . Figure 12a shows a plan view of the model. The yellow areas have an induced magnetization as a consequence of a magnetic susceptibility of 0.01 SI. The blue body has only a magnetization of 0.4 A/m and an inclination of -90° , which is intended to generate a more symmetric anomaly equivalent to being at the pole. The red body has a stronger magnetization of 0.48 A/m and an inclination in the opposite direction ($+90^\circ$), which is intended to represent a situation in which there is strong reversed remanent magnetization. The top of all bodies is at the surface, the bottom is at 600 m, and the magnetic sensor is 100 m above the surface. The yellow bodies are elongated in the north–south direction and east–west direction to understand the impact of size on the transformation. The magnetic data are shown in Figure 12b. The yellow bodies all show a north–south asymmetry, with a blue low to the south and a yellow high to the north (the appearance of sun shading from the north is an optical illusion, a consequence of the color bar used having yellow highs that are brighter than the blue lows). The blue body in the top-right corner has a more symmetric magnetic field, with a central high and blue lows around at least three sides. The red body in the top left has a central low and is surrounded by a yellow high on at least three sides. All four yellow bodies below have similar magnetic susceptibilities, and the total field for these four bodies is displayed as a similar shade of green in the center. The anomalies on the edges are larger on the north and south edges, as the direction perpendicular to strike and magnetic field is roughly in the same direction, so the coupling factor c defined in the first paragraph of the “Apparent susceptibility estimation” section has the value $c = 1$, but on the west and east edges, $c \cong 0.75$, so these edge anomalies are smaller. As the magnetic field in the center of each yellow body is comparable, we conclude that the strike direction is only significant near the edges. The top right (blue) body is more yellow, as the remanent magnetization of this body is larger than the induced magnetization

of the yellow bodies, and the top left (red) body has a magnetic field that is deep blue, as the remanent anomaly is strongly negative.

The magnetic field is then transformed to the pole and vertical dip using equation 11 where $T_0^{\beta=0}$ is defined in equation 20. Then, the apparent susceptibility (Figure 12c) is calculated by dividing the transformed magnetic field by $2\pi Fc$, except the strike direction

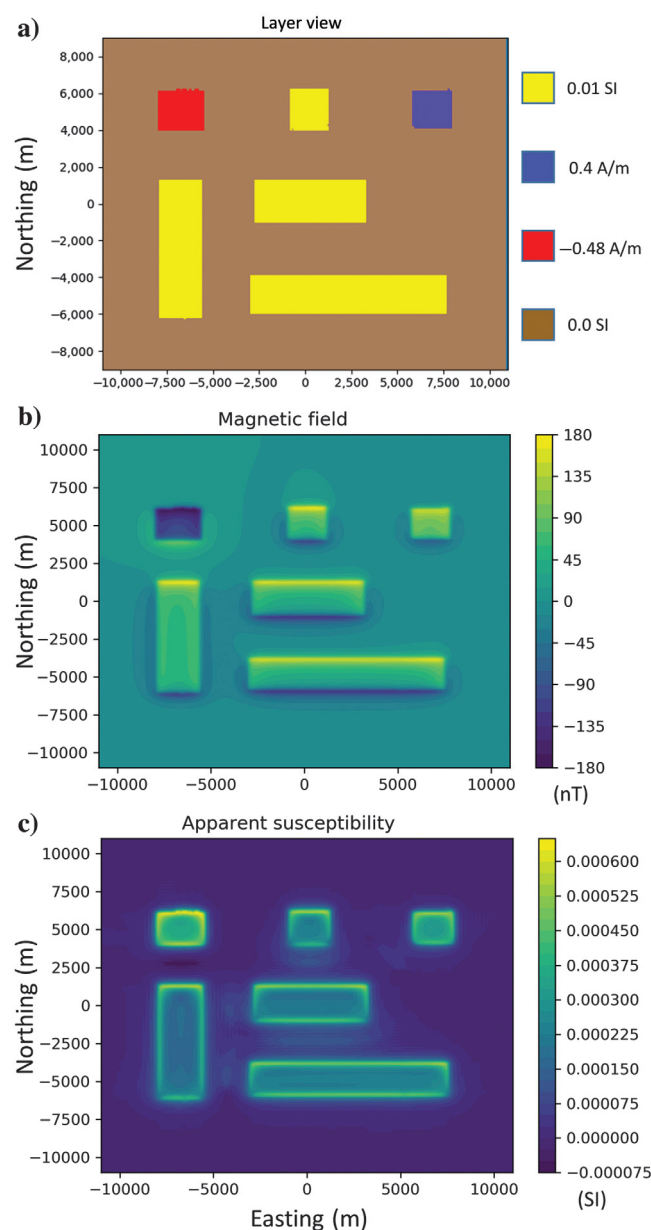


Figure 12. (a) Plan view of the synthetic model. The yellow bodies have susceptibilities of 0.01 SI and an inducing field of 50,000 nT inclined at -60° and a declination of 5° . The blue body has a remanent magnetization of 0.4 A/m as if the body was at the pole, and the red body has a stronger remanent magnetization (0.48 A/m), the same inclination, but the opposite direction, as if the magnetization was reversed. The bodies extend from surface to 600 m depth. (b) The magnetic field of the model. (c) The apparent susceptibility after (1) the field has been transformed to the pole and vertical dip using equation 11 with the tilt defined in equation 20, and then (2) normalizing this transformed field by $2\pi Fc$.

varies over the area, so we have set $c = 1$, so the value will be approximate and might differ with strike direction, particularly near the edges. In all cases, the asymmetries are reduced, with yellow

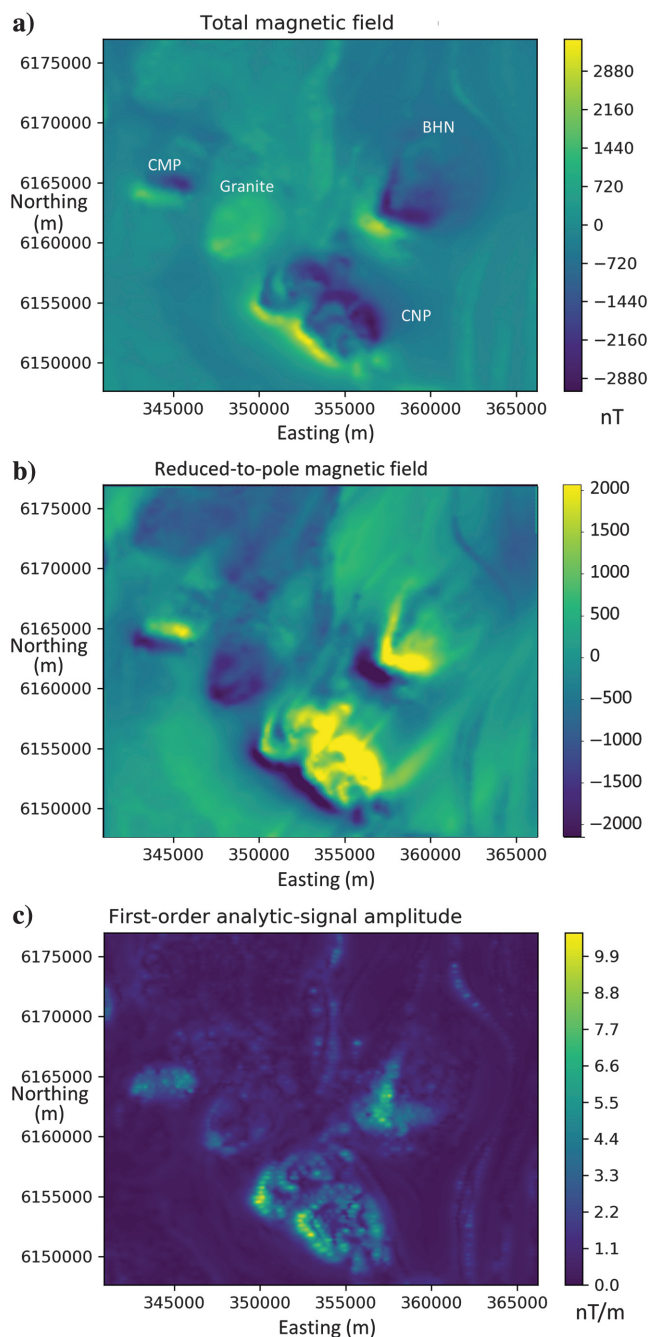


Figure 13. (a) The total magnetic field in the Black Hill area north of Mannum, South Australia, showing strongly asymmetric anomalies indicating remanent magnetization oriented northeast–southwest. (b) The magnetic data reduced to the pole assuming all magnetization are in the direction of the remanent magnetization (similar to Rajagopalan et al., 1995). (c) The first-order ASA of the data in (a), with highs outlining the edges of the magnetic bodies. Black Hill is 100 km east–northeast of Adelaide, South Australia. The eastings and northings are in zone 54S, and the datum is GDA94.

susceptibility highs marking the edges of each body. In their centers, the yellow bodies have a similar tone of green for the apparent susceptibility, corresponding to approximately 0.0003 SI. This is a factor of 30 less than the true susceptibility, but this is because the depth extent of the model is only 600 m, but an infinite depth extent is assumed for the apparent susceptibility model, so an underestimate is expected. A further reduction in the estimate is a consequence of the flying height being 100 m, but 0 m is assumed. The magnetic anomalies of the infinite depth extent bodies on the profiles in Figures 6 and 7 (also with susceptibilities of 0.01 SI) are approximately 3000 nT, and the thinner bodies on the grid have anomalies of approximately 100 nT, being less by a factor of approximately 30 and explaining the discrepancy between the apparent and actual susceptibilities. The apparent susceptibility of the top right body is a lighter shade of yellow, closer to 0.0004 SI, and the top left body has a susceptibility closer to 0.0005 SI, which is expected as the remanence of this left body is greater.

One additional synthetic example is presented in Appendix A.

FIELD EXAMPLE — THE BLACK HILL NORITE

The Black Hill intrusive bodies, located 50 km north of Mannum, South Australia, are a well-studied example of strong remanent magnetization. Although the lithology is commonly referred to as norite, Rajagopalan et al. (1995) say the lithologies of the bodies include peridotites, troctolites, olivine gabbros, norites, gabbro-norites, pyroxene monzonites, and posttectonic granites. The intrusives have a strong remanent magnetization of approximately 4.9 A/m, the outcrop magnetic susceptibility measurements range from 0.02 to 0.05 SI, and the Koenigsberger ratio is approximately 2 (Rajagopalan et al., 1995).

Magnetic data over the area were acquired by the Bureau of Mineral Resources (now Geoscience Australia) using a line spacing of 1500 m and a flight height of 150 m (Rajagopalan et al., 1995). The data have been gridded with a grid spacing of 98.8 m. The magnetic map is shown in Figure 13a, with the anomalies associated with four intrusive bodies identified by Rajagopalan et al. (1995). The Black Hill norite (BHN) has a dipolar anomaly below the BHN label, with a high to the south and west and a strong low to the immediate north and east of these highs. At this magnetic latitude, weak lows are expected to the south and larger highs to the north, so this anomaly clearly shows remanent magnetization. For the BHN anomaly, the lows to the north weaken slowly to the northeast, which Foss and McKenzie (2011) interpret as being due to a plunge or a thinning to the northeast. The Cambrai pluton (CMP) below the CMP label has a dipolar anomaly with an east–west trend, with the strongest high to the southwest and the low to the northeast. The Central pluton (CNP) to the west of the CNP label has several highs to the southwest and lows approximately 3 km to the northeast. All three of these anomalies show remanent magnetization in a similar orientation. A purely positive anomaly between the CNP and CMP anomalies was identified by Rajagopalan et al. (1993) as a granite intrusive and interpreted to have a different remanence direction by Foss and McKenzie (2011).

Reduction to the magnetic pole is problematic (Rajagopalan, 2003). When the magnetization is assumed to be induced in the direction of the earth's field, the reduced-to-pole image generated assuming only induced magnetization is only subtly different from the original image in Figure 13a. Hence, Rajagopalan et al. (1995) reduce the Black Hill magnetic data to the pole assuming that the magnetization was in the

remance direction, which had previously been determined by taking oriented samples in the field and measuring the magnetization in the laboratory. The BHN, CNP, and CMP all have similar remanent magnetization directions with an inclination of 7.6° and a declination of 221° . The reduced-to-pole results were reasonable for these three bodies (regenerated in Figure 13b). The three bodies still show a small negative to the southwest, and there are some artifacts evident in the declination direction, even though an amplitude correction inclination of -60° was used in the Geosoft RTP algorithm. The total magnetization vector for the granite body is different, so the pole-reduced data are dominated by a low over the body, which is not expected for a reduced-to-pole anomaly. Estimating the remanence direction does not always require field and laboratory work; Phillips (2005) and Foss and McKenzie (2011) describe methods for estimating the remanence direction from the magnetic data. However, the estimates from these methods do not always agree with the field/laboratory measurements and their methods will work better when the remanence is significantly stronger than the induced magnetization.

Rajagopalan et al. (1995) also present an ASA_1 image, similar to that in Figure 13c. This image can be generated without knowing the remanence direction and is expected to have highs over the edges of bodies, which it does for the CNP and granite, but the BHN only really has highs on the southern and western edges. The CMP is a single high on ASA_1 , which Foss and McKenzie (2011) attribute to the fact that it is a compact body. This image shows some noise associated either with gridding or the flight lines. Some careful filtering could reduce this noise, but we have left it in to illustrate the inherent noise associated with calculating ASA_1 . Foss and McKenzie (2011) point out that the lighter blue feature on the eastern edge of the image that runs north–south is distorted around the BHN.

Figure 14a shows a map of ASA_0 for this area. This map is similar to ASA_1 , but the noise is not as evident, because the Hilbert transform filter does not amplify the higher frequencies as derivatives do. However, the features appear spatially broad and out of focus compared with ASA_1 and the total field. This broadening is a consequence of the Hilbert transforms of the total field decreasing in amplitude slowly away from the edges of the body (as is also evident in Figures 6 and 7). This broad character can be reduced by transforming the data to the data that would be measured at the pole with vertical dip. When transforming the data by the sine of $T_0^{\beta=0}$, we found it was not necessary to apply a soft threshold. In the synthetic studies, the thresholding was necessary in areas where there were no magnetic sources but the field data show magnetic sources across the whole map area.

The apparent susceptibility shown in Figure 14b is created by normalization of the transformed magnetic field by the factor $2\pi Fc$. As the total field in the area is not listed in the cited literature and the vintage of the data is not known, the total field in the area cannot be precisely calculated from the international geomagnetic reference field (GRF) or the definitive GRF. Hence, we have somewhat arbitrarily used a value of $F = 50,000$ nT. There are three further inaccuracies: (1) that the strike direction varies, so c will vary across the map, but we have assumed $c = 1$ everywhere, (2) that the depth extent is unlikely to be infinite, and (3) that the sensor height is above the top of the body. Hence, the susceptibilities will not be exact, but they can still be used for comparison and qualitative interpretation. The reduced-to-pole and vertical dip image looks identical to the apparent susceptibility image, except the value on the color bar should be multiplied by $2\pi F$ (314,159 nT).

On the apparent susceptibility map, there are several areas with strong negative values, which is not possible in theory, so these could be a consequence of some of our assumptions being incorrect (e.g., 2D bodies or that $T_0^{\beta=0} = -T_{ASA_0}$). However, it is most likely an artifact of interference, because the strongest negative in the synthetic grid example (Figure 12c) occurs midway between the red body and the yellow body to the immediate south, where the interference is expected to be greatest. The CMP feature on the far west appears as a simple compact body trending east–west and has a moderate susceptibility. The granite body just to the east of the CMP has a slightly weaker apparent susceptibility and the susceptibility is relatively uniform over the whole body, largely being a uniform shade of turquoise. Interestingly, there are no ridges outlining the edges of the CMP and the granite, as we see in the synthetic data. The CNP body in the central south of the area has a much more complex character, appearing to be made up of two circular features, a larger one to the southeast and a smaller one to the northwest. Within these two features, the shapes of the highs and lows suggest multiple pulses of intrusives. The larger magnetic susceptibility values around the edges could be a pulse of more magnetic magma, or the edges of the bodies, as seen in the synthetic

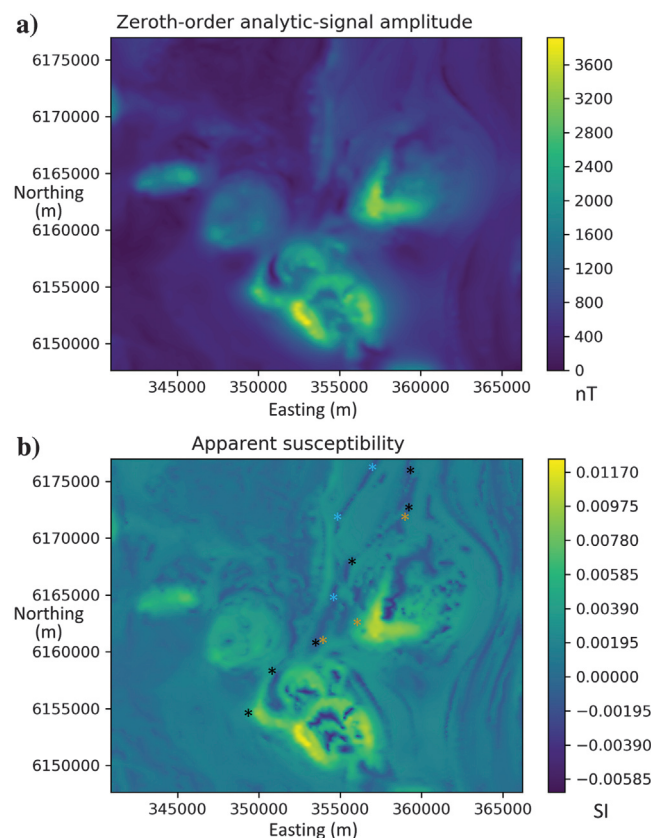


Figure 14. (a) The ASA_0 map of the data in Figure 13a. (b) The apparent susceptibility of the total magnetization calculated by (1) transformation of the data in (a) to the pole and vertical dip using equation 11 and a tilt defined in equation 20, and (2) normalizing by $2\pi Fc$. A line joining the black asterisks shows the location of a shear zone interpreted by Foss and McKenzie (2011). Other zones not interpreted by Foss and McKenzie (2011) but clearly evident in (b) are two possible splays along lines made by connecting the light blue and dark brown asterisks, respectively.

Table 1. Summary of the quantities used to transform data to the pole and vertical dip.

| | ASA | Tilt angle | Mapped quantity | |
|--|--|---|--|--|
| | | | Formula for reconstructing the mapped quantity from ASA and tilt angle | Formula for reconstructing mapped quantity for $\beta = 0$ |
| Vertical derivative of the field $\partial H/\partial z$ | $ASA_1 = \sqrt{\left(\frac{\partial H}{\partial x}\right)^2 + \left(\frac{\partial H}{\partial z}\right)^2}$ | $T_1 = \tan^{-1}\left(\frac{\partial H}{\partial z} / \frac{\partial H}{\partial x}\right)$ | $\frac{\partial H}{\partial z} = ASA_1 \sin(T_1)$ | $\frac{\partial H}{\partial z} = ASA_1 \sin\left(\frac{\pi}{2} - T_{ASA_1}\right)$ |
| Magnitude of the magnetic field H | | | $H = ASA_0 \sin(T_0)$ | $H = ASA_0 \sin(-T_{ASA_0})$ |

data. The BHN body to the east has a strong apparent susceptibility in the southwest corner, but not elsewhere, suggesting that either the body is thicker or shallower here or there is a pulse of more magnetic material in this corner. There are distinct features that can be identified in the rocks surrounding the magmatic intrusions. The light blue feature pointed out on the eastern edge of Figure 13c is more clearly evident in Figure 14b, and there are multiple similar features, both to the east of the BHN and also to the south and northwest. These are likely showing slightly different magnetic susceptibilities in the metasediments of the surrounding country rocks of the Kanmantoo Group. The shear zone interpreted by Foss and McKenzie (2011), which was interpreted touching the northwest edge of the CNP and the BHN, also can be identified and located quite easily on the apparent susceptibility image. Our interpretation of its location is shown in Figure 14b along the line joining together the black asterisks. However, other structures could have been interpreted, such as along the pathway marked by light blue or dark brown asterisks, which could be splays of the shear zone.

Other features are more apparent on the susceptibility image. One is the tree-like structure sprouting northward from the area between CMP and the granite. This could be a bedrock structure, but it might be a drainage feature filled with more magnetic material. The other feature is the pockmark appearance that occurs in several places, particularly in and around the BHN and the granite body. This texture could possibly indicate that the intrusives extend beyond the zones of high susceptibility, or they could reflect xenoliths on the edges of the intrusive bodies.

DISCUSSION

The calculation of ASA_0 always has a positive value, so the direction of the total magnetization is lost. However, comparing Figure 12b and 12c suggests a way of identifying remanence and estimating the total magnetization direction. For example, subtracting the field in Figure 12b from the field used to derive Figure 12c could be used to indicate the direction of the total magnetization. Of course, this is approximate and assumes vertical dip.

In the grid examples, ASA_0 is transformed to the total field at the pole with zero dip, rather than transforming ASA_1 to the vertical derivative at the pole with zero dip. This was done, because it is not straightforward to determine the correct sign of the transformed vertical derivative on the different edges of the bodies. One possible way to estimate the sign is to transform to the total field at the pole and vertical dip and then calculate the vertical derivative of this quantity. This could be compared with the vertical derivative transformation from the measured ASA_1 . If the signs of the two vertical

derivatives differ, then the sign of the vertical derivative calculated by transformation from ASA_1 should be reversed. Some type of median or alpha-trimmed median filtering of the field might be necessary around the locations where the signs change.

The apparent susceptibility is a useful image to interpret because it gives an idea of the susceptibility of the rock and this can help in distinguishing different lithologies or magnetic mineral content. The method that we describe here for calculating the apparent susceptibility does not have the same issues as calculating the susceptibility using the traditional RTP method in cases when there is remanent magnetization present. The method provides an *apparent* susceptibility value that incorporates the total magnetization (induced plus remanent) and not just the induced magnetization.

CONCLUSION

Using the ASAs and an appropriate transforming tilt, it is possible to transform the data to be the data that would be measured at the pole if the bodies had a vertical dip (Table 1). If the first-order ASA_1 and a phase-reflected tilt of the first-order ASA, $T_1^{\beta=0} = \pi/2 - T_{ASA_1}$, is used for the transformation, then the field is the vertical derivative; but if the zeroth-order ASA_0 , is used with the negative of the tilt of the zeroth-order ASA, $T_0^{\beta=0} = -T_{ASA_0}$, in the transformation, then the transformed field is an approximate total field.

The resulting approximate field can be transformed to an apparent susceptibility that would be consistent with the total magnetization. The transformed field or the apparent susceptibility produces an image that is easy to interpret and shows features not clearly evident on other presentations of the data.

ACKNOWLEDGMENTS

We are grateful to C. Foss (CSIRO) for providing us with the Black Hill data set. Funding for this work was through a Discovery Grant provided by the Natural Sciences and Engineering Research Council of Canada (NSERC). R.S. Smith would also like to dedicate this work to his mother, M. Smith (née Sando), who worked on a nearby magmatic body that also intruded into the Kanmantoo Group.

DATA AND MATERIALS AVAILABILITY

Data associated with this research are available and can be obtained by contacting the corresponding author.

APPENDIX A

BISHOP SYNTHETIC EXAMPLE

A further demonstration of our method can be seen in its application to the Bishop synthetic data set, available from (Anonymous, 2016) where the data set is also described in detail. This data set was generated for the purposes of testing algorithms for determining the depth to the magnetic basement (Williams et al., 2002, 2005; Fairhead et al., 2004). The model is an unmagnetized sedimentary basin above a magnetic basement, with the depth to basement varying from approximately 1 km in the northwest to more than 9 km in the southeast, as shown in Figure A-1a. There are some gradual and some sudden changes in the depth and these will result in lateral contrasts in the magnetic susceptibility and will have a corresponding magnetic anomaly. At the same time, there are changes in the magnetic

susceptibility of the units in the basement; Figure A-1b shows the susceptibility of the basement, as supplied for the Bishop model in cgs units $\times 10^{-6}$. There are three packages, running approximately east–west across the areas. The southern package has a susceptibility of 1000×10^{-6} cgs, the central package has a higher value of 3000×10^{-6} cgs, and the northern package is 2000×10^{-6} cgs. There are also four intrusive bodies. The largest one on the boundary of the central and the southern package has a susceptibility of 8000×10^{-6} cgs. The other intrusive bodies have susceptibilities of 5000×10^{-6} cgs; one is on the boundary of the northern and central package and the other two are entirely within the southern package.

The magnetic response of the model for the case when the magnetic inclination is 30° is shown in Figure A-1c. The intrusives in the basement have dipolar anomalies, with positive anomalies to the south and negative anomalies to the north. The central package has a positive anomaly on its southern edge and trends downward to a negative anomaly on the northern edge. There are anomalies associated with the changes in depth of the basement. The strongest of these is the large and sudden change in depth that runs east–west in the middle of the southern package. The north–south-trending changes in basement depth are poorly coupled to the north–south field, so they are expected to have their strongest anomalies where there are offsets in these features. The zeroth-order ASA (Figure A-1d) shows strong symmetric anomalies associated with all four intrusives and there are highs along the north and south boundaries of the central package. Within the central package, the amplitude is generally larger, appearing as a lighter green shade than the other packages. There are some linear anomalies associated with the changes in basement depth and some more discrete anomalies, most evident on the west edge in the central package. The first-order ASA (Figure A-1e) shows the changes in basement depth and the edges of the packages. There are discrete features associated with the shallow features on the western edge of the area and the intrusive bodies generally have their edges highlighted as well. The largest intrusive body has been broken into five features, corresponding to where the edges are trending more east–west than north–south because these edges couple more strongly to the magnetic field. The southwest intrusive is narrower and trends east–west, so it appears as a single feature on this image.

The apparent susceptibility image, shown in Figure A-1f, shows the edges of the central package and also has the central package as a lighter shade of green than the other packages, consistent with its larger susceptibility. The central package is not green in the zone between the two intrusive bodies, but this is expected, because this is the deepest part of the basement, so susceptibility estimates will be less as the magnetic field is attenuated. It is not possible

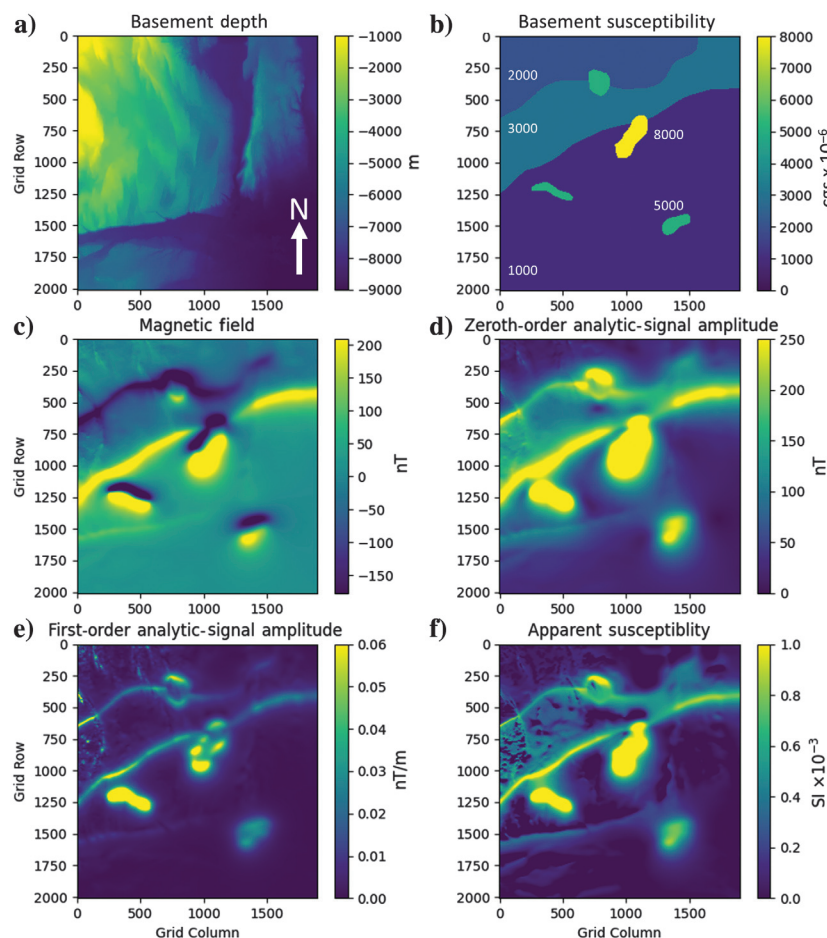


Figure A-1. (a) The depth to the magnetic basement below the sedimentary basin in the Bishop model. (b) The susceptibility of the basement material, with the susceptibilities of the three east–west packages labeled on the left side in $\times 10^{-6}$ cgs. There are four intrusive bodies, the largest one is the most susceptible (8000×10^{-6} cgs) with the other three green bodies having susceptibilities of 5000×10^{-6} cgs. (c) The magnetic field of the model, when the inclination is 30° . (d) The zeroth-order ASA, note that the asymmetry of the anomalies has been removed, but the anomalies are quite wide. (e) The first-order ASA, also with no asymmetry, primarily showing the edges of the bodies. Within the central package, the magnitude of ASA_1 looks similar to the south and north packages. The three wide intrusives to the east also have their edges highlighted. (f) The apparent susceptibility, with the central package showing as more susceptible, and the four intrusives appear as more compact than that they do on the zeroth-order analytic-signal-amplitude image. A grid north arrow is shown on (a).

to identify a difference in susceptibility of the north and south packages, because the susceptibilities are too low. Isolated susceptible features are evident along the west and northern edge where the basement is shallower and coincident with the changes in the basement depth. Due to the depth of the basement, the apparent susceptibilities are not expected to agree precisely with the actual values; however, some qualitative agreement is seen. For example, the apparent susceptibility of the most susceptible body (the large central intrusive) has the largest apparent susceptibilities, with values approximately 1.5×10^{-3} SI; the intrusive to the southwest has an apparent susceptibility of 1.4×10^{-3} SI and the one to the southeast has values of 0.7×10^{-3} SI. These differences can be attributed to differences in the basement depth, as the southwest intrusive is approximately 2000 m deep, whereas the southeast one is closer to 8000 m deep. The northern intrusive has a susceptibility in its center of approximately 0.7×10^{-3} SI, which is very roughly half the apparent susceptibility of the central intrusive, which approximates the ratio of the true susceptibility shown in Figure A-1b. Some of the intrusives have higher apparent susceptibility values on the edges (like the synthetic data in Figure 12), but others do not (like the field data in Figure 14). Despite the variability in the depth, the apparent susceptibility image is most like the basement apparent susceptibility and is thus a suitable image to interpret if the character of the basement is the information the interpreter wishes to extract from the data.

REFERENCES

- Abramowitz, M. A., and I. A. Stegun, 1972, Handbook of mathematical functions with formulas, graphs, and mathematical tables: U.S. National Bureau of Standards, Applied Mathematics Series 55.
- Anonymous, 2016, Bishop model, https://wiki.seg.org/wiki/Bishop_Model, accessed 21 December 2021.
- Arkani-Hamed, J., 1988, Differential reduction-to-the-pole of regional magnetic anomalies: *Geophysics*, **53**, 1592–1600, doi: [10.1190/1.1442441](https://doi.org/10.1190/1.1442441).
- Arkani-Hamed, J., 2007, Differential reduction to the pole: Revisited: *Geophysics*, **72**, no. 1, L13–L20, doi: [10.1190/1.2399370](https://doi.org/10.1190/1.2399370).
- Baranov, V., 1957, A new method for interpretation of aeromagnetic maps: Pseudo-gravimetric anomalies: *Geophysics*, **22**, 359–382, doi: [10.1190/1.1438369](https://doi.org/10.1190/1.1438369).
- Baranov, V., and H. Naudy, 1964, Numerical calculation of the formula of reduction to the magnetic pole: *Geophysics*, **29**, 67–79, doi: [10.1190/1.1439334](https://doi.org/10.1190/1.1439334).
- Cole, P., 2021, PyGMI, <https://patrick-cole.github.io/pygmi/>, accessed 21 December 2021.
- Cooper, G., 2016, The downward continuation of the tilt angle: *Near Surface Geophysics*, **14**, 385–390, doi: [10.3997/1873-0604.2016022](https://doi.org/10.3997/1873-0604.2016022).
- Cooper, G. R. J., 2019, Filtering potential field data by modifying its amplitude and phase in the space domain: *Geophysical Prospecting*, **67**, 455–464, doi: [10.1111/1365-2478.12722](https://doi.org/10.1111/1365-2478.12722).
- Dean, W. C., 1958, Frequency analysis for gravity and magnetic interpretation: *Geophysics*, **23**, 97–127, doi: [10.1190/1.1438457](https://doi.org/10.1190/1.1438457).
- Donoho, D. L., 1995, De-noising by soft-thresholding: *IEEE Transactions on Information Theory*, **41**, 613–627, doi: [10.1109/18.382009](https://doi.org/10.1109/18.382009).
- Fairhead, J. D., S. E. Williams, and G. Flanagan, 2004, Testing magnetic local wavenumber depth estimation methods using a complex 3D test model: 74th Annual International Meeting, SEG, Expanded Abstracts, 742–745, doi: [10.1190/1.1851313](https://doi.org/10.1190/1.1851313).
- Foss, C., and B. McKenzie, 2011, Inversion of anomalies due to remanent magnetisation: An example from the Black Hill norite of South Australia: *Australian Journal of Earth Sciences*, **58**, 391–405, doi: [10.1080/08120099.2011.581310](https://doi.org/10.1080/08120099.2011.581310).
- Guspi, F., and I. Novara, 2009, Reduction to the pole and transformations of scattered magnetic data using Newtonian equivalent sources: *Geophysics*, **74**, no. 5, L67–L73, doi: [10.1190/1.3170690](https://doi.org/10.1190/1.3170690).
- Hansen, R. O., and R. S. Pawlowski, 1989, Reduction to the pole at low latitudes by Wiener filtering: *Geophysics*, **54**, 1607–1613, doi: [10.1190/1.1442628](https://doi.org/10.1190/1.1442628).
- Isles, D. J., and L. R. Rankin, 2013, Geological interpretation of aeromagnetic data: Australian Society of Exploration Geophysicists, <https://www.aseg.org.au/publications/geological-interpretation-aeromagnetic-data>, accessed 15 November 2020.
- Keating, P., and L. Zerbo, 1996, An improved technique for reduction to the pole at low latitudes: *Geophysics*, **61**, 131–137, doi: [10.1190/1.1443933](https://doi.org/10.1190/1.1443933).
- Li, Y., M. Nabighian, and D. W. Oldenburg, 2014, Using an equivalent source with positivity for low-latitude reduction to the pole without striation: *Geophysics*, **79**, no. 6, J81–J90, doi: [10.1190/geo2014-0134.1](https://doi.org/10.1190/geo2014-0134.1).
- Li, Y., and D. W. Oldenburg, 2001, Stable reduction to the pole at the magnetic equator: *Geophysics*, **66**, 571–578, doi: [10.1190/1.1444948](https://doi.org/10.1190/1.1444948).
- Li, Y., J. Sun, S.-L. Li, and M. Leão-Santos, 2021, A paradigm shift in magnetic data interpretation: Increased value through magnetization inversions: *The Leading Edge*, **40**, 89–98, doi: [10.1190/le40020089.1](https://doi.org/10.1190/le40020089.1).
- Lu, R. S., 1998, Finite-impulse-response reduction-to-the-pole filter: *Geophysics*, **63**, 1958–1964, doi: [10.1190/1.1444489](https://doi.org/10.1190/1.1444489).
- Lu, R. S., J. Mariano, and D. E. Willen, 2003, Differential reduction of magnetic anomalies to the pole on a massively parallel computer: *Geophysics*, **68**, 1945–1951, doi: [10.1190/1.1635048](https://doi.org/10.1190/1.1635048).
- MacLeod, I. N., K. Jones, and T. F. Dai, 1993, 3D analytic signal in the interpretation of total magnetic field data at low magnetic latitudes: *Exploration Geophysics*, **24**, 679–687, doi: [10.1071/EG993679](https://doi.org/10.1071/EG993679).
- Mendonça, C. A., and J. B. C. Silva, 1993, A stable truncated series approximation of the reduction-to-the-pole operator: *Geophysics*, **58**, 1084–1090, doi: [10.1190/1.1443492](https://doi.org/10.1190/1.1443492).
- Miller, H. G., and V. Singh, 1994, Potential field tilt — A new concept for location of potential field sources: *Journal of Applied Geophysics*, **32**, 213–217, doi: [10.1016/0926-9851\(94\)90022-1](https://doi.org/10.1016/0926-9851(94)90022-1).
- Nabighian, M. N., 1972, The analytic signal of two-dimensional magnetic bodies with polygonal cross-section: Its properties and use for automated anomaly interpretation: *Geophysics*, **37**, 507–517, doi: [10.1190/1.1440276](https://doi.org/10.1190/1.1440276).
- Nabighian, M. N., 1984, Toward a three-dimensional automatic interpretation of potential field data via generalized Hilbert transforms: Fundamental relations: *Geophysics*, **49**, 780–786, doi: [10.1190/1.1441706](https://doi.org/10.1190/1.1441706).
- Phillips, J. D., 2005, Can we estimate magnetization directions from aeromagnetic data using Helbig's integrals? *Earth Planets Space*, **57**, 681–689, doi: [10.1186/BF03351848](https://doi.org/10.1186/BF03351848).
- Rajagopalan, S., 2003, Analytic signal vs. reduction to pole: Solutions for low magnetic latitudes: *Exploration Geophysics*, **34**, 257–262, doi: [10.1071/EG03257](https://doi.org/10.1071/EG03257).
- Rajagopalan, S., D. Clark, and P. Schmidt, 1995, Magnetic mineralogy of the Black Hill norite and its aeromagnetic and palaeomagnetic implications: *Exploration Geophysics*, **26**, 215–220, doi: [10.1071/EG995215](https://doi.org/10.1071/EG995215).
- Rajagopalan, S., P. Schmidt, and D. Clark, 1993, Rock magnetism and geophysical interpretation of the Black Hill norite, South Australia: *Exploration Geophysics*, **24**, 209–212, doi: [10.1071/EG993209](https://doi.org/10.1071/EG993209).
- Reeves, C., 2005, Aeromagnetic surveys: Principles, practice and interpretation: *Geosoft/Seequent*, https://pages.mtu.edu/~jdiehl/Homework4550/Aeromagnetic_Survey_Reeves.pdf, accessed 27 November 2020.
- Reford, M. S., 1964, Magnetic anomalies over thin sheets: *Geophysics*, **29**, 532–536, doi: [10.1190/1.1439388](https://doi.org/10.1190/1.1439388).
- Roest, W. R., J. Verhoef, and M. Pilkington, 1992, Magnetic interpretation using the 3D analytic signal: *Geophysics*, **57**, 116–125, doi: [10.1190/1.1443174](https://doi.org/10.1190/1.1443174).
- Salem, A., S. Williams, J. D. Fairhead, D. Ravat, and R. Smith, 2007, Tilt-depth method: A simple depth estimation method using first-order magnetic derivatives: *The Leading Edge*, **26**, 1502–1505, doi: [10.1190/1.2821934](https://doi.org/10.1190/1.2821934).
- Silva, J. B. C., 1986, Reduction to the pole as an inverse problem and its application to low-latitude anomalies: *Geophysics*, **51**, 369–382, doi: [10.1190/1.1442096](https://doi.org/10.1190/1.1442096).
- Smith, R. S., J. B. Thurston, T.-F. Dai, and I. N. MacLeod, 1998, iSPITM — The improved source parameter imaging method: *Geophysical Prospecting*, **46**, 141–151, doi: [10.1046/j.1365-2478.1998.00084.x](https://doi.org/10.1046/j.1365-2478.1998.00084.x).
- Thurston, J. B., and R. S. Smith, 1997, Automatic conversion of magnetic data to depth, dip, and susceptibility contrast using the SPI(TM) method: *Geophysics*, **62**, 807–813, doi: [10.1190/1.1444190](https://doi.org/10.1190/1.1444190).
- Williams, S., J. D. Fairhead, and G. Flanagan, 2002, Realistic models of basement topography for depth to magnetic basement testing: 72nd Annual International Meeting, SEG, Expanded Abstracts, 814–817, doi: [10.1190/1.1817384](https://doi.org/10.1190/1.1817384).
- Williams, S. E., D. Fairhead, and G. Flanagan, 2005, Comparison of grid Euler deconvolution with and without 2D constraints using a realistic 3D magnetic basement model: *Geophysics*, **70**, no. 3, L13–L21, doi: [10.1190/1.1925745](https://doi.org/10.1190/1.1925745).

Biographies and photographs of the authors are not available.